Journal of Solar Energy Research (JSER)

Journal homepage: www.jser.ut.ac.ir

Design and Fabrication of a Multi-Junction Hybrid Heterostructure Based on ZnO/CuO/PS/Si for Advanced Optoelectronic Applications

Jenan Saddam[a], Muneer H. Jaduaa[a,*]

[a]*Physics Department, College of Science, University of Wasit, Wasit, Iraq.*

ARTICLE INFO

Article Type:

Research Article

Received:21.07.2025
Accepted:03.08.2025

Keywords:
Hybrid heterojunction;
Nanoparticles;
Doping;
Efficiency;
Solar cell

A B S T R A C T

The study designs a vertically stacked Ag:ZnO/CuO/PS/Si hybrid heterojunction to enhance optoelectronic performance through material synergy and Ag doping. ZnO, CuO, and Ag structures were analyzed; the Ag:ZnO layer was doped at 3%, 5%, and 7% and deposited on porous silicon. Structural tests showed average crystallite sizes of 25.20 nm (Ag), 31.42 nm (CuO), and 35.16 nm (ZnO). AFM revealed the smoothest surface at 3% Ag (Sq = 19.11 nm), while 5% and 7% were less smooth. Optical band gaps showed quantum confinement: 2.37 eV (Ag), 3.57 eV (CuO), 3.71 eV (ZnO). The device with 7% Ag achieved the highest efficiency (0.3125) and Pmax (27.60 μW). The 5% sample had 0.1027 efficiency and 9.09 μW Pmax, and 3% had 0.0964 and 8.68 μW. Results indicate lower doping yields smoother surfaces reducing recombination, while higher Ag content improves optical response and transport, boosting photovoltaic performance.

1. Introduction

The development of heterostructure materials has revolutionized high-performance optoelectronic devices. [1], including photodetectors, solar cells, and light-emitting diodes. Hybrid multi-junction heterostructures, composed of alternating layers of metals, semiconductors, and nanostructured interfaces [2], offer unique pathways to engineer electronic band structures, enhance charge separation, and optimize light absorption across a wide spectral range[3, 4].

[*]*Corresponding Author Email: malzubaidy@uowasit.edu.iq*

Cite this article: Saddam, J. and Jaduaa, M. (2025). Design and Fabrication of a Multi-Junction Hybrid Heterostructure Based on ZnO/CuO/PS/Si for Advanced Optoelectronic Applications. Journal of Solar Energy Research, 10(1), 2161-2175. doi: 10.22059/jser.2025.398689.1599

DOI: 10.22059/jser.2025.398689.1599

In this context, combining silver (Ag), zinc oxide (ZnO), copper oxide (CuO), porous silicon (PS), and crystalline silicon (Si) into a single vertically aligned multi-layered heterostructure is highly beneficial [5].Each component offers distinct functional advantages. Ag functions as a highly conductive electrode and enhances plasmonic effects. ZnO, a wide-bandgap n-type semiconductor with excellent optical transparency and electron mobility, acts as an efficient electron transport layer [6, 7]. CuO, a p-type narrow-bandgap semiconductor, offers strong absorption in the visible range and supports hole transport. [8]. Porous silicon provides a high surface area, facilitating effective interface coupling and light trapping, while bulk silicon serves as a foundational photonic substrate. [9, 10]. Reducing bulk silicon dimensions to nanoparticles (PS) leads to marked changes in optical, electrical, and electronic properties [11, 12].

This combination contributes to increasing interfacial engineering, carrier dynamics, and photonic interactions can be precisely tuned. Multi-junction architectures based on such diverse materials can achieve enhanced photogeneration efficiency through built-in electric fields at each interface, enabling charge carrier separation and directional transport with minimized recombination losses [13, 14].

Despite their individual use in optoelectronic research, their integration into a unified, functionally graded, and vertically aligned stack remains largely unexplored [15]. This work aims to design, fabricate, and characterize such a hybrid structure using cost-effective deposition techniques. The focus will be on investigating structural, morphological, optical, and electrical characteristics, emphasizing understanding interfacial behavior and performance implications for optoelectronic applications.[16, 17].

This study contributes to the growing field of hybrid nanostructured junctions and paves the way for developing next-generation photonic and electronic systems.

Naderi et al. [18] formulated the new epitaxial bottom-up deposition technique of nanostructured ZnO thin film on porous silicon substrates. The experiment involved improving optoelectrical performances by incorporating porous silicon and nanostructured ZnO as a source for photovoltaic applications. The findings showed a significant enhancement of the produced devices' light absorption efficiency and electrical conductivity. This study will develop green energy sources in an innovative way of solar cell production using nanomaterials.

Alrasheedi, N.H. [19], conducted a study titled "The Effects of Porous Silicon and Silicon Nitride Treatments on the Electronic Qualities of Multicrystalline Silicon for Solar Cell Applications." The study examined the synergistic effect of using porous silicon and silicon nitride layers on a multicrystalline silicon substrate in solar cells. The properties of untreated wafers (reflectance of about 40%, carrier lifetime of approximately 8 microseconds) were compared to those with SiN treatment (reflectance of about 7%, carrier lifetime of roughly 71 microseconds) and a combination of SiN_6 and PSi. The PSi+SiN_1 showed the best performance with around 3% reflectance, a carrier lifetime of about 1041 microseconds, an auxiliary length of 676 micrometers, and a recombination velocity of 1.6 cm/sec. This result highlights the effectiveness of incorporating porous silicon for surface passivation to enhance solar cell efficiency.

Hasani, E [20]. studied the SCAPS-1D simulation to design the ZnO/CuO/Cu 2Se heterojunction solar cells utilizing systematic parameter tuning of the layer thicknesses and doping concentrations. The Cu2Se layer enhanced light-harvesting rates compared to the conventional binary structures in the near-infrared area. Finer analysis suggested the best configurations that can be used to get better power conversion efficiencies through band alignment engineering. This was a theoretical foundation for generating future generation high-performance characteristics of eco-friendly thin-film solar cells

The novelty of this work is the strategic design and manufacture of a vertically-oriented multi-junction hybrid heterostructure comprising Ag-doped ZnO, CuO, porous silicon and crystalline silicon layer. Contrary to past works that explored these materials either separately or in combinations, this study carefully looks into incorporation of these materials and their graded silver doping (3% 5% 7%) into a single unified multilayered structure and studies their influence on optoelectronic properties. It is helpful to mention that pulsed laser ablation and use of silver nanoparticles as well as their inclusion in ZnO host systems can be utilized to implement localized surface plasmon resonance (LSPR) enhancement processes that have not been explored in many light-based PS-based systems. In addition, the morphological (AFM, SEM), structural (XRD), and optical (UV-Vis, Tauc) investigations make it possible to understand the relationship between the level of doping, surface texture, and photovoltaic effect comprehensively. The current research points to a new direction of controlling the interface to optimize the solar conversion efficiency in hybrid

devices utilizing material synergy and plasmonic engineering.

2. Materials and Methods

This study employed a multi-step experimental protocol to design and fabricate a vertically integrated multi-junction hybrid heterostructure composed of Ag-doped ZnO, CuO, porous silicon (PS), and crystalline silicon (Si) (Ag: ZnO/CuO/PS/Si) layers. The methodology comprises five main stages:

2.1. Synthesis of Nanomaterials

Copper Oxide (CuO) Nanoparticles were synthesized via a simple wet chemical precipitation method by reacting 0.2 M copper (II) chloride ($CuCl_2$) with 1 M sodium hydroxide (NaOH) at 70 °C under magnetic stirring. The resulting precipitate was filtered and redispersed to ensure homogeneity [21].

Zinc Oxide (ZnO) Nanoparticles were prepared similarly by reacting zinc nitrate hexahydrate $Zn(NO_3)_2 \cdot 6H_2O$ with NaOH under identical conditions, producing a white ZnO precipitate [22].

Silver Nanoparticles (AgNPs) were fabricated using the pulsed laser ablation method (PLA), in which a 1000 mJ Nd: YAG laser at 8 Hz irradiated a high-purity silver target submerged in deionized water, producing a colloidal Ag solution [23].

2.2. Preparation of Hybrid Thin Film Solutions

ZnO was mixed with AgNPs in different weight ratios (ZnO: Ag = 97:3, 95:5, and 93:7) using a vortex mixer to ensure uniform dispersion.

CuO, ZnO, and ZnO: Ag mixtures were prepared for spray deposition.

2.3. Substrate Preparation

Glass Substrates: They are cleaned with deionized water and ethanol and treated in an ultrasonic bath before drying and heating at 150 °C.

Silicon Substrates: n-type single-crystal Si wafers were etched using a photo-electrochemical etching (PEE) process in an HF-ethanol solution under illumination, creating porous silicon (PS) layers to enhance light trapping and interfacial surface area [24].

2.4. Thin Film Deposition

Thin films were sequentially deposited on glass and porous silicon substrates at 150 °C using thermal spray pyrolysis.

- First, CuO was deposited on PS/Si.
- Second layers consisted of pure ZnO or ZnO: Ag solutions (in three different Ag concentrations).
- The final structure was capped with Ag electrodes using silver paste to complete the sandwich configuration:
- ZnO/CuO/PS/Si
- (3%Ag:ZnO)/CuO/PS/Si
- (5%Ag:ZnO)/CuO/PS/Si
- (7%Ag:ZnO)/CuO/PS/Si

2.5. Structural and Optical Characterization

The structural properties of the prepared thin films were examined using X-ray diffraction (XRD, Shimadzu XRD-6000) to identify the crystal phases and assess crystallinity. Surface morphology and grain distribution were investigated through Field Emission Scanning Electron Microscopy (FE-SEM) and Atomic Force Microscopy (AFM), providing insights into the nanoscale topography and uniformity of the films. Fourier Transform Infrared Spectroscopy (FTIR, Shimadzu 8400S) analyzed functional groups and chemical bonding. Optical properties, including absorbance, transmittance, and bandgap energy, were evaluated using UV-Vis spectrophotometry. Electrical and photovoltaic performance was assessed by measuring current–voltage (I–V) characteristics under dark and illuminated conditions (100 mW/cm² using a 100 W halogen lamp at 30 cm). Key parameters such as open-circuit voltage (Voc), short-circuit current (Isc), maximum power (Pmax), fill factor (FF), and conversion efficiency (η) were extracted to determine the effectiveness of the fabricated hybrid solar cells.

3. Results and discussion

3.1 X-ray Diffraction (XRD)

The crystalline structure and phase purity of the synthesized Ag, CuO, and ZnO nanoparticles were examined using X-ray diffraction (XRD). The resulting diffractograms and crystallographic parameters are summarized in Figures 1, 1,2, and 3, as well as Tables 1, 1,2, and 3.

3.1.1 Silver Nanoparticles (Ag)

The XRD pattern of silver nanoparticles, shown in Figure 1, displays prominent diffraction peaks at 2θ = 38.10°, 64.40°, and 77.30°, corresponding to the (111), (220), and (311) planes, respectively, of face-centered cubic (FCC) silver, in accordance with the standard ICDD card No. 04-0783. The high intensity of the (111) peak indicates preferred orientation along this crystallographic plane. Additionally, the crystallite size was determined using the Debye-Scherrer equation [25].

$$D = \frac{K\lambda}{\beta \cos\theta} \quad (1)$$

where D is the crystallite size, K is the shape factor (0.94 for spherical structures), λ is the X-ray wavelength, β is the full width at half maximum (FWHM) of the diffraction peak, and θ is the Bragg angle [13, 26-28]

The calculated crystallite sizes with a mean value of 25.20nm, indicating nanoscale crystallinity as shown in Table 1.

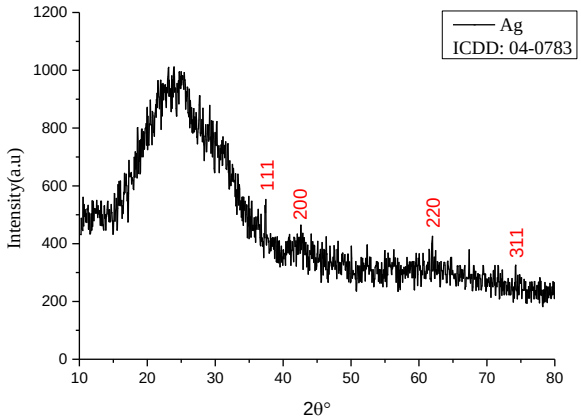

Figure 1. XRD pattern of Ag nanoparticles

Table 1. Crystallite size calculations for Ag based on peak broadening

2 θ (Deg.)	FWHM (Deg.)	Crystallite size (nm)	Average Crystallite size (nm)
38.10	0.35	24.01	25.20
44.30	0.35	24.51	
64.40	0.35	26.82	
77.40	0.40	25.45	

3.1.2 Copper Oxide Nanoparticles (CuO)

The XRD pattern for CuO, shown in Figure 2, displays characteristic peaks at 2θ = 32.50°, 38.70°, and 53.50°, which correspond to the (110), (002), and (202) planes of monoclinic CuO, confirming the presence of single-phase CuO (ICDD card No. 45-0937). The broad peaks indicate a nanocrystalline structure. The calculated crystallite sizes based on FWHM values are summarized in Table 2, with an average of 31.42 nm.

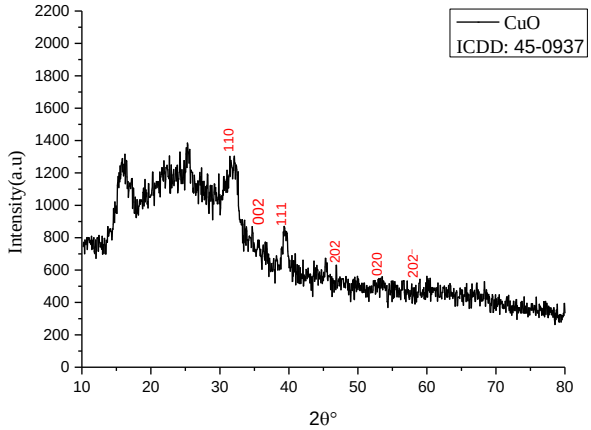

Figure 1 . XRD pattern of CuO nanoparticles

Table 2. Crystallite size calculations for CuO

2θ (Deg.)	FWHM (Deg.)	Crystallite size (nm)	Average Crystallite size (nm)
32.50	0.25	33.10	31.42
35.50	0.26	32.08	
38.70	0.27	31.18	
48.70	0.28	31.14	
53.50	0.29	30.68	
58.30	0.30	30.32	

3.1.3 Zinc Oxide Nanoparticles (ZnO)

Figure 3 shows the XRD pattern of ZnO nanoparticles. Sharp and strong peaks at 2θ = 31.77°, 36.25°, 56.60°, and 67.96° correspond to the (100), (101), (110), and (112) planes, respectively, of hexagonal wurtzite ZnO, matching ICDD card No. 36-1451. The lack of secondary phases indicates high purity. The crystallite sizes calculated for the ZnO sample are listed in Table 3, with an average size of

35.16 nm, slightly larger than those of Ag and CuO, possibly due to ZnO's thermal stability and larger grain growth during synthesis conditions.

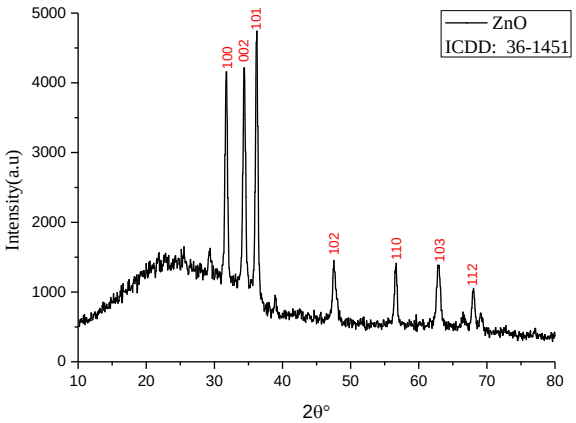

Figure 2. XRD pattern of ZnO nanoparticles

Table 3. Crystallite size calculations for ZnO

2θ (Deg.)	FWHM (Deg.)	Crystallite size (nm)	Average Crystallite size (nm)
31.77	0.35	23.60	
34.42	0.38	21.89	
36.25	0.35	23.88	
47.54	0.34	25.53	24.95
56.60	0.35	25.78	
62.86	0.35	26.60	
67.96	0.35	27.37	

3.2 E-SEM analysis results

The surface morphology and particle size distribution of the synthesized nanomaterials were analyzed using Field Emission Scanning Electron Microscopy (FE-SEM) at magnifications of 70,000× and 135,000×. The results closely match the crystallite sizes estimated from X-ray diffraction (XRD), confirming the nanoscale nature of the materials. Figure 4 shows the morphology of silver (Ag) nanoparticles. The particles appear relatively spherical and show some degree of agglomeration. The average grain size measured was approximately 25.57 nm, which is in good agreement with the crystallite size obtained from XRD analysis (≈25.20 nm, Table 1).

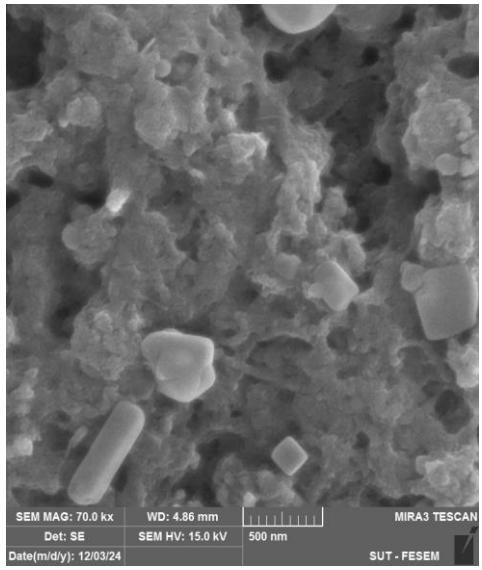

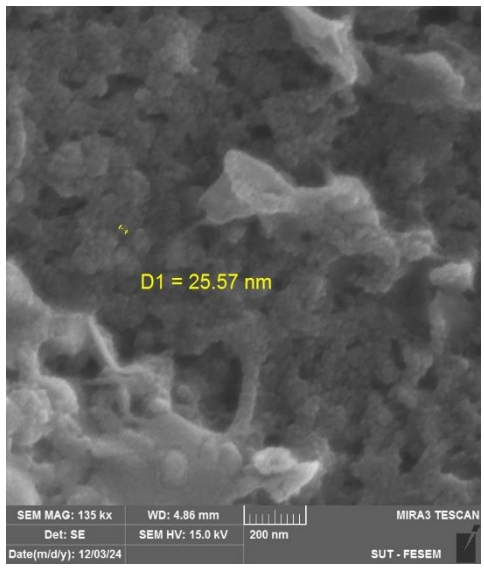

Figure 3. FE-SEM Images of Ag Nanoparticles

Figure 5 shows the surface morphology of the CuO sample, which is more granular and porous than Ag. The nanoparticle sizes fall within the 35.52 nm range, and the fine, nearly spherical granules indicate good dispersion. These observations are in agreement with the XRD results (Figure 2), which confirmed monoclinic CuO with an average crystallite size of 31.42 nm (Table 2). The relatively uniform distribution of particles further supports the homogeneity of the CuO thin film, which is critical for enhancing charge transport in heterojunction configurations.

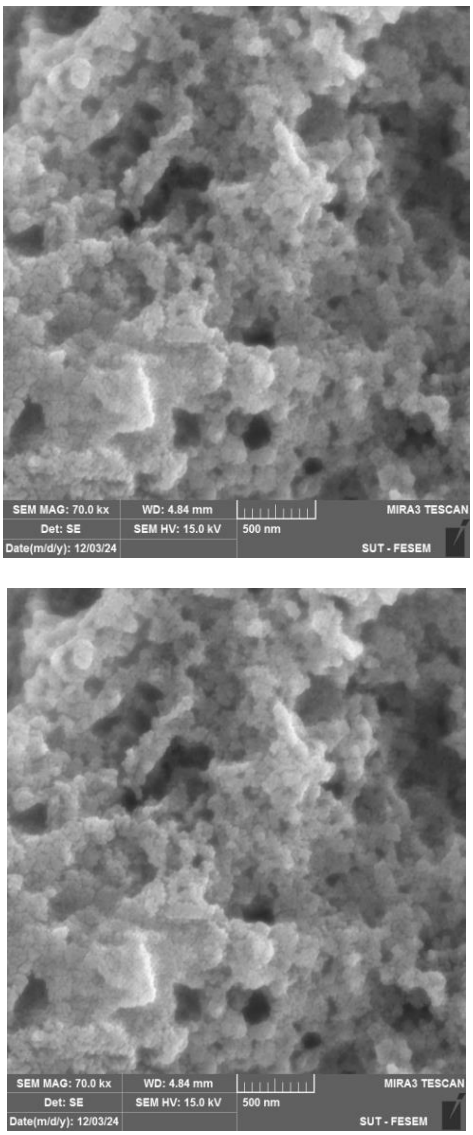

Figure 4. FE-SEM Images of CuO Nanoparticles

Figure 6 shows that the ZnO nanostructure exhibits a dense, polyhedral morphology with clear grain boundaries. The measured particle size is approximately 26.26 nm, which complements the average crystallite size obtained from XRD (≈24.95 nm, Table 3). The well-defined grain formation and tight packing are consistent with the highly crystalline wurtzite phase identified by sharp XRD peaks at (100), (002), and (101) orientations Figure 3. This morphological coherence supports efficient optical absorption and electron transport, essential for optoelectronic applications.

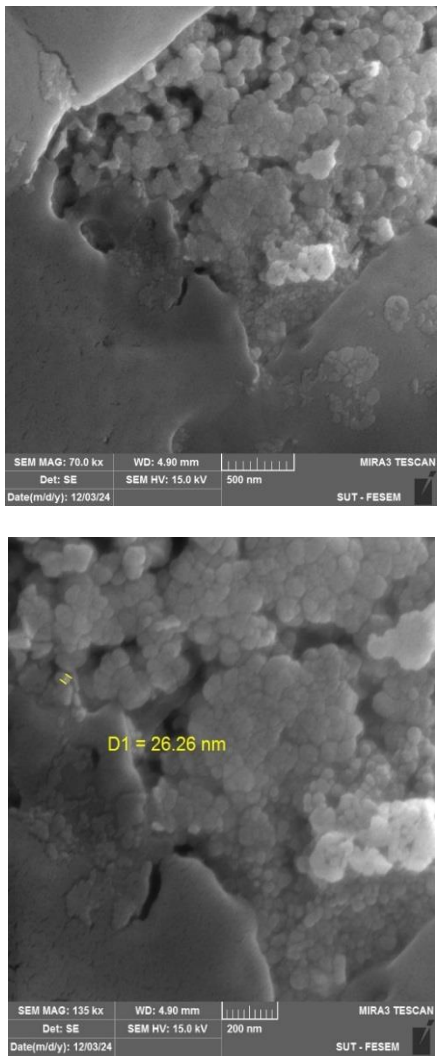

Figure 5. FE-SEM Images of ZnO Nanoparticles

The FE-SEM analysis confirmed the nanostructured nature of Ag, CuO, and ZnO materials, with 25–35 nm particle sizes. These findings agree with XRD-derived crystallite sizes, validating the successful synthesis of uniform nanocrystalline films suitable for integration into hybrid heterojunction solar cell architectures.

3.3 AFM Topography and Surface Roughness Analysis

Atomic Force Microscopy (AFM) was conducted to evaluate the 3D surface morphology and quantify the nanoscale roughness of Ag, CuO, and ZnO thin films over a 2.0 × 2.0 μm² scan area. The height distributions, surface roughness (Sq), and peak

topographies are compared in light of crystallite and particle size data from XRD and FE-SEM.

3.3.1 Silver (Ag) Thin Film

The AFM image in Figure 7 reveals distinct protrusions with Z-heights up to ~99 nm. The surface exhibits a granular, moderately rough texture with a measured root mean square roughness (Sq) of 19.11 nm. In the leveled image Figure 8, the grain peaks become more uniformly distributed across the surface, while the histogram Figure 9 indicates a peak frequency around 100 nm with minor dispersion.
These results confirm the presence of discrete, moderately rough nanostructures. This is consistent with the FE-SEM data showing average particle sizes ~25.6 nm and XRD-derived crystallite size of ~25.20 nm, indicating that the Ag layer consists of polycrystalline grains forming surface protrusions that enhance surface plasmon behavior.

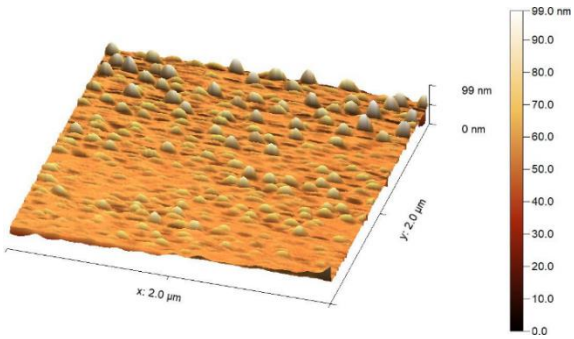

Figure 6. 3D AFM surface plot of Ag nanoparticles over a 2 × 2 µm² scan area, showing grain peaks up to 99 nm in height.

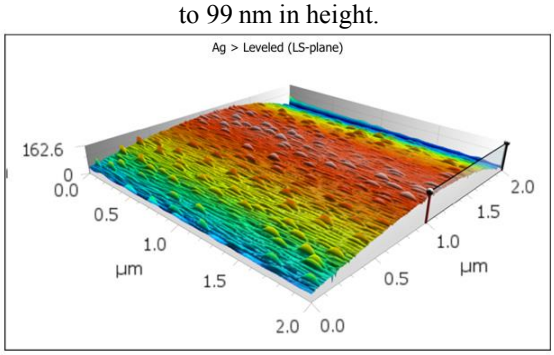

Figure 7. Leveled AFM Image (Z-Height up to ~162 nm)

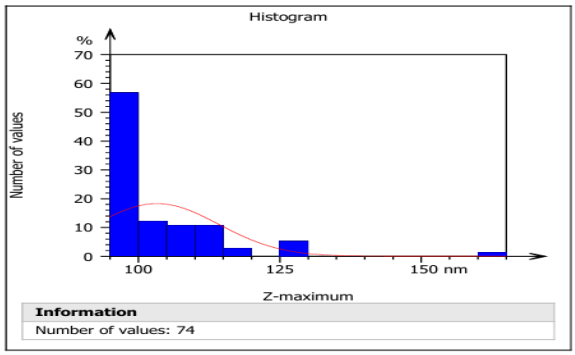

Figure 8. Height Distribution Histogram of Nanoparticles

3.3.2 Copper Oxide (CuO) Thin Film

The CuO film, shown in Figure 10, displays a relatively more uniform and densely packed surface morphology. The maximum vertical height reaches ~41 nm, with an Sq value of 9.397 nm, the lowest among the three films. The leveled surface, Figure 11, confirms this smooth topography, and the histogram, Figure 12, shows most Z-values concentrated around 60–65 nm.

This smoother morphology strongly agrees with the XRD data (crystallite size ≈ 31.42 nm) and SEM images, which showed evenly dispersed grains. The low roughness suggests that CuO forms a compact, continuous film with minimal agglomeration — a desirable characteristic for charge transport layers in optoelectronic devices.

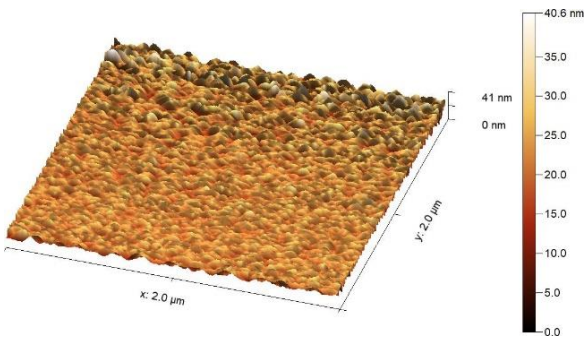

Figure 9. 3D AFM surface plot of Ag nanoparticles over a 2 × 2 µm² scan area, showing grain peaks up to 40 nm in height

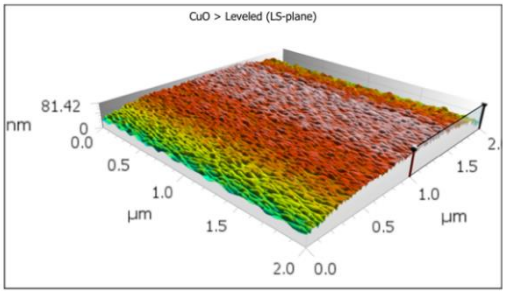

Figure 10. Leveled AFM Image (Z-Height up to ~81.42 nm)

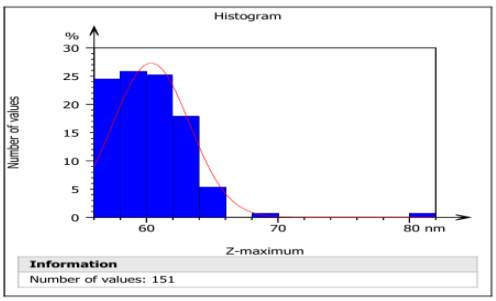

Figure 11. Height Distribution Histogram of Nanoparticles

3.3.3 Zinc Oxide (ZnO) Thin Film

The ZnO surface exhibits a significantly higher surface roughness. Figure 13 illustrates an uneven, highly textured surface with peak heights up to 167 nm. The SQ value for ZnO was measured at 79.49 nm, the highest among all samples. The leveled AFM image, Figure 14, further emphasizes the variation in surface elevation, while the histogram, Figure 15, shows a broad Z-max distribution extending up to ~600 nm. This pronounced roughness suggests the formation of clustered ZnO grains or vertical columnar growth, which aligns with the highly crystalline XRD pattern Figure 3 and FE-SEM images showing dense grain boundaries. While high roughness may enhance light scattering and absorption in optoelectronic devices, it could also influence the uniformity of subsequent layers in multi-junction architectures.

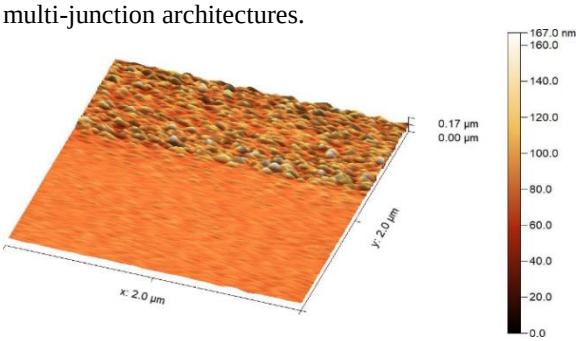

Figure 12. 3D AFM surface plot of Ag nanoparticles over a 2 × 2 µm² scan area, showing grain peaks up to 167nm in height

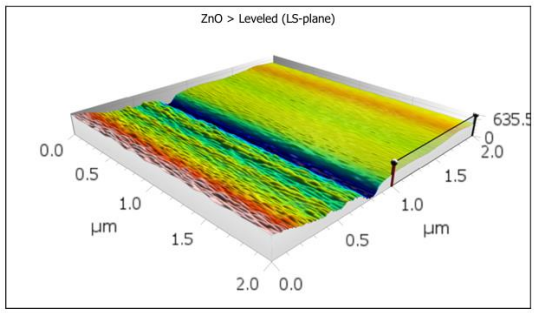

Figure 13. Leveled AFM Image (Z-Height up to ~635.5 nm)

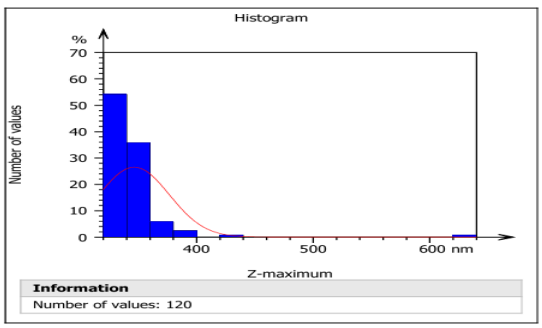

Figure 14. Height Distribution Histogram of Nanoparticles

3.4 Optical Band Gap Analysis Based on Tauc Plots

The optical band gap energies (Eg) of Ag, CuO, and ZnO thin films were evaluated using Tauc plots derived from UV-Vis absorption spectra. The plots represent the relationship between $(\alpha h\nu)^2$ and photon energy ($h\nu$), assuming direct allowed electronic transitions. The linear portion of each curve was extrapolated to intersect the energy axis, revealing the corresponding optical band gap.

Figure 16 shows the UV-Vis absorption spectrums of three different nanoparticles: silver nanoparticle (Ag), copper oxide nanoparticle (CuO) and zinc oxide nanoparticle (ZnO). These spectra are recorded between 200 and 1000nm. The black, red and blue curves are Ag, CuO and ZnO, respectively.

Each of the three materials has a strong absorption in the ultraviolet range (200300 nm), a sharp slope as the wavelength goes longer, a characteristic of semiconductors with a large band gap, and that of metallic nanoparticles experiencing surface plasmon resonance (Ag). The deep UV region with a

maximum absorbance has interband electronic transitions or a plasmonic excitation.

Ag spectrum (black) contains a sharper, more intense peak in the UV range, possibly because of localized surface plasmon resonance (LSPR), a familiar characteristic of noble metal nanoparticles. Red CuO and blue ZnO are semiconducting oxides, which exhibit high absorbances in the UV range due to intrinsic band-to-band transitions.[29].

Beyond 400 nm, the absorbance decreases to insignificance in all samples, which shows that the samples are transparent in the visible and near-IR wavelengths. Comparative spectral behaviour indicates that Ag has different plasmonic characteristics, whereas ZnO and CuO follow transitions related to the band gap, which can be further calculated through Tauc analysis to acquire the optical band gap.

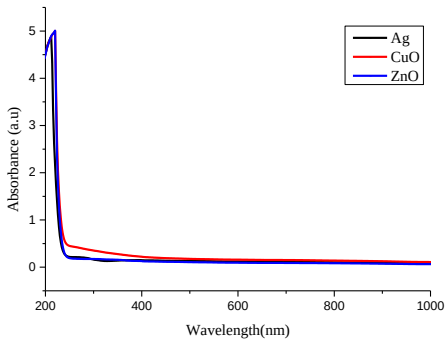

Figure 15. The experimental optical absorbance curve of silver nanoparticles (Ag – CuO and ZnO NPs)

Figure 17 presents the Tauc plot for silver (Ag) nanoparticles. A distinct linear region is observed, and the extrapolation of this region yields an optical transition energy of approximately 2.37 eV. Although silver is a metallic material and does not exhibit a conventional band gap, this value represents interband transitions arising from electronic excitations between the d-band and the sp-conduction band. The appearance of this feature is influenced by the nanostructured nature of the film, where quantum confinement and surface plasmon resonance effects significantly modify the optical behaviour. These phenomena are typical in Ag nanostructures and are strongly supported by complementary structural data (e.g., XRD and AFM), indicating fine particle distribution and nanoscale morphology.

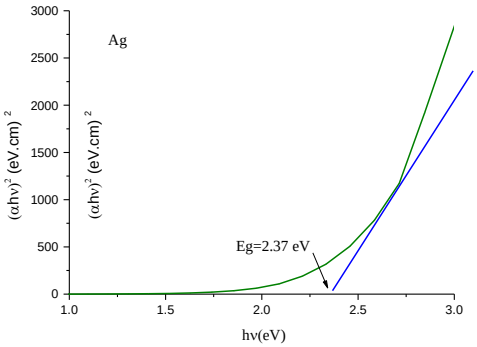

Figure 16. Tauc plot of Ag thin film showing an optical band gap of 2.37 eV due to interband transitions in nanostructured silver.

The Tauc plot depicted in Figure 18 clearly shows that a straight line exists, which, on further extension, intersects the graph of energy at 3.57 eV. This value is ascribed to the quantum size effect in the nanocrystalline films, and is significantly higher than the standard bulk range of CuO. An increase in band gap energy indicates that either very small-sized crystals exist or that surface and interface states interact with the material due to the nanoscale film production method. The structural characterizations, including the 31.4 nm crystal size deduced by XRD, and low surface roughness by the AFM (Sq = 9.397 nm), support the interpretation that quantum confinement and smoothness of the film are also involved in the optical properties seen.

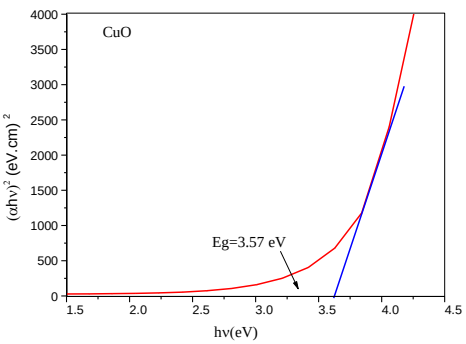

Figure 17. Tauc plot of CuO thin film indicating a band gap of 3.57 eV, attributed to quantum confinement effects.

As shown in Figure 19, the ZnO film exhibits an optical band gap of 3.71 eV, notably larger than the standard bulk value (~3.3 eV). This blue shift is commonly associated with quantum confinement in nanocrystalline ZnO and surface defects or strain.

The AFM analysis revealed a relatively high surface roughness (Sq = 79.49 nm), and the XRD results confirmed a wurtzite crystal structure with a crystallite size of ~35.2 nm, which together support this optical behavior.

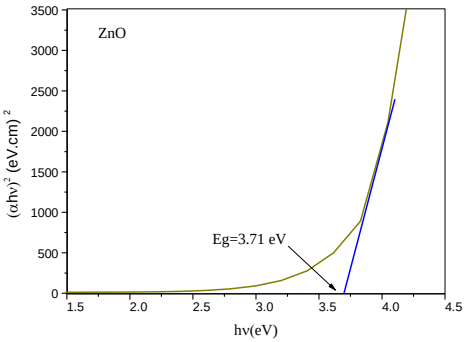

Figure 18. Tauc plot of ZnO thin film showing a band gap of 3.71 eV, reflecting nanocrystalline behavior and surface effects

A comparative Tauc plot on the optical absorption behavior of Ag (green), CuO (red), and ZnO (yellow) thin films is presented in Figure 20. The optical transition energies are estimated at 2.37eV, 3.57eV and 3.71eV corresponding to Ag, CuO and ZnO, respectively. Such deviations of the typical bulk behavior emphasize the significant role of nanoscale structuring, quantum size effects and effects of the interfaces. The information shows that the three materials have altered optical characteristics when deposited as nanostructured films. As such, the materials are promising candidates for UV photodetectors, plasmonics, and optics. The fact that the obtained optical data and the structural/morphological analyses are almost entirely in agreement confirms the high quality of the obtained films and the possibility of tuning the films.

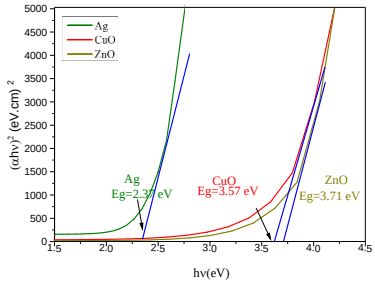

Figure 19. Combined Tauc plots of Ag, CuO, and ZnO films highlighting their enhanced optical band gaps

The optical transition energies determined experimentally (Ag: 2.37 eV, CuO: 3.57 eV, ZnO: 3.71 eV) show some noticeable deviation of the measured values when compared to the bulk material, proving to a large extent that quantum confinement and surface effects are playing a significant role together with the nanoscale structural characteristics of the samples. These findings agree with previous outcomes of structural (XRD), morphological (SEM, AFM) and surface roughness characterizations, substantiating that well-characterized nanostructured films with customizable optical properties have been prepared.

3.5 Photovoltaic Performance Analysis of Ag-Doped Hybrid Junctions (3%, 5%, 7%)

Figure 21 shows a series of Ag/(ZnO: Ag)/CuO/PS/Si/Ag hybrid heterojunction solar cells that were fabricated and characterized, with a focus on the effect of varying silver doping levels (3%, 5%, and 7%) within the ZnO matrix on the overall photovoltaic behavior. Comprehensive current–voltage (I–V) measurements under standard illumination conditions were performed, and the results were analyzed in terms of key performance indicators, including short-circuit current (Isc), open-circuit voltage (Voc), maximum power point (Vm × Im), fill factor (FF), and efficiency (η).

The results indicate that the device doped with 7% Ag delivered the highest overall photovoltaic efficiency (η = 0.3125), along with a fill factor of 45.09%, a maximum voltage of 2300 mV, and a photocurrent of 12 μA at the maximum power point. This superior performance is attributed to enhanced charge carrier separation and collection facilitated by localized surface plasmon resonance (LSPR) effects from the higher concentration of metallic Ag nanoparticles. These particles effectively increase the local electromagnetic field, leading to stronger light–matter interaction and improved photon harvesting.

In contrast, the 5% Ag-doped device showed a more moderate efficiency of 0.1027 and a reduced fill factor of 15.88%, indicating a suboptimal balance between morphological smoothness and carrier transport properties. The 3% Ag sample, which demonstrated the smoothest surface morphology observed in AFM analysis (Sq = 19.11 nm), presented a fill factor of 32.26% and efficiency of 0.0964. Although smoother surfaces are known to reduce recombination sites and facilitate better charge extraction, the relatively lower current and voltage output suggest that insufficient plasmonic

enhancement limited the device's ability to generate and collect charge carriers efficiently.

Table 4 shows the photovoltaic characteristics of solar cells with different percentage concentrations of silver (Ag) of 3%, 5% and 7%. Those parameters are short-circuit current (Isc), open-circuit voltage (Voc), current at maximum power (Im), voltage at maximum power (Vm), fill factor (FF), and conversion efficiency (η). With 3% Ag, the cell has an Isc of 24.0 mA and a Voc of 1121 mV, which yields a fill factor of 32.26 % and a low efficiency of 0.0964 %. Raising the concentration of Ag to 5 percent reduces the Isc to 21.0 µA and increases the Voc to 2770 mV and the Vm to 1010 mV, but the fill factor is lower, 15.88%. The efficiency increases a little to 0.1027% although FF is less. Surprisingly, the 7% Ag-doped sample also provides the overall best performance record, having a Voc of 3300 mV, Im of 120, and Vm of 2300 mV, thus a considerably high fill factor of 45.09% and a conversion efficiency of 0.3125%. This implies that higher contents of Ag boost the performance of the devices in utilizing solar energy, particularly at 7 percent doping, which probably occurs because of dynamic charges and decreased recombination losses within the device structure.

Table 4. Voc, Isc, Pmax, FF, and efficiency of solar cells with 3%, 5%, and 7% Ag doping. The 3% Ag device shows the best performance

Sample	Isc (µA)	Voc (mV)	Im (µA)	Vm (mV)	FF (%)	η
3% Ag	24.0	1121	9	93	32.26	0.0964
5% Ag	21.0	2770	9	1010	15.88	0.1027
7% Ag	18.9	3300	12	2300	45.09	0.3125

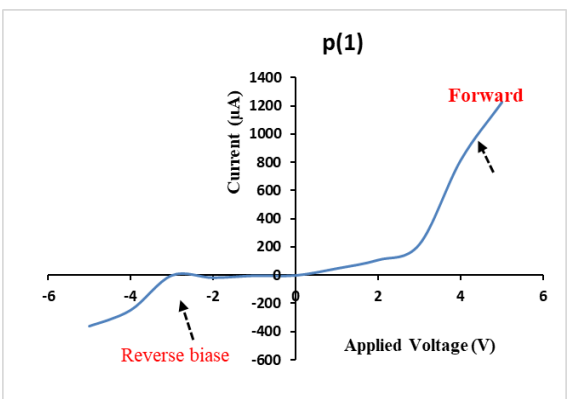

A: I–V curve for 3% Ag-doped hybrid junction

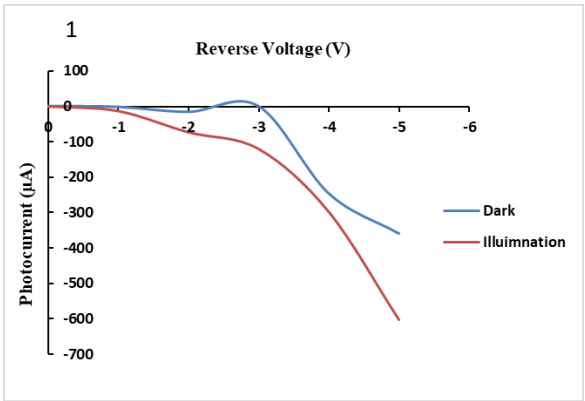

B: P–V curve for 3% Ag-doped hybrid junction

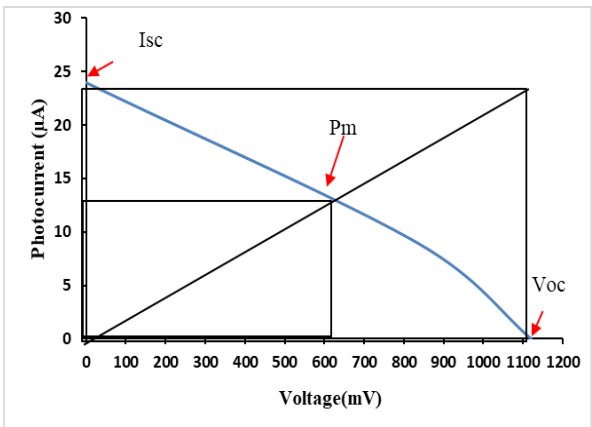

C: I–V and P–V curves for the 3% Ag-doped solar cell, showing Isc, Voc, and maximum power point (Pm)

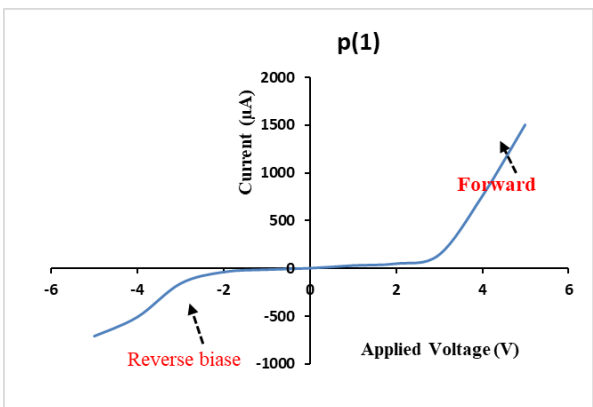

D: I–V curve for 5% Ag-doped hybrid junction

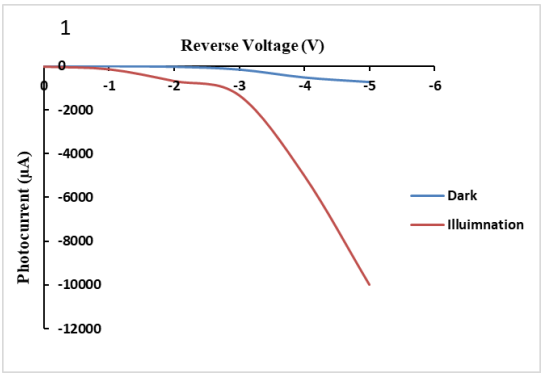

E :P–V curve for 5% Ag-doped hybrid junction

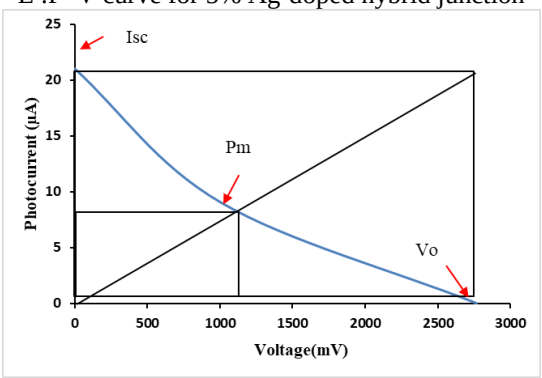

F: I–V and P–V curves for the 5% Ag-doped solar cell, highlighting Isc, Voc, and maximum power point (Pm)

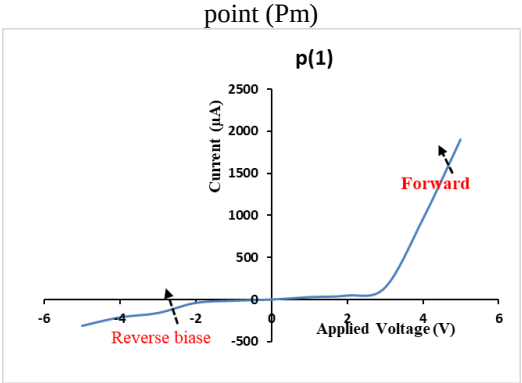

G: I–V curve for 7% Ag-doped hybrid junction

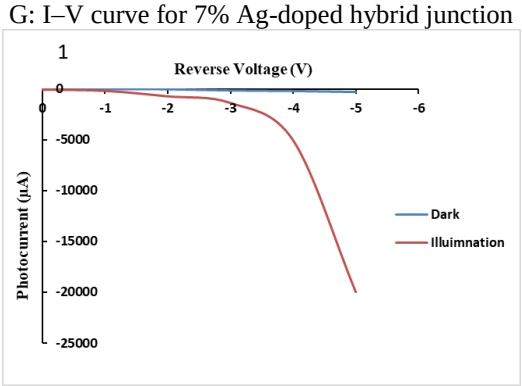

H :P–V curve for 7% Ag-doped hybrid junction

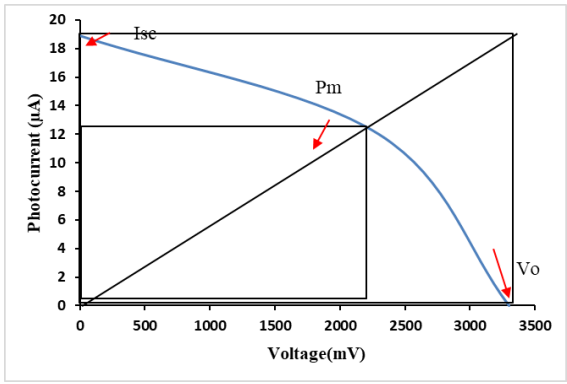

I: The I–V and P–V curves for the 7% Ag-doped solar cell indicate Isc, Voc, and maximum power point (Pm)

Figure 20. Electrical and power output behavior of the fabricated hybrid solar cells with Ag-doped ZnO. The 3% Ag-doped structure consistently outperformed the 5% and 7% samples in all key photovoltaic metrics

4. Conclusions

Integrating ZnO, CuO, and Ag into a hybrid heterojunction on porous silicon significantly improved the optoelectronic characteristics of the fabricated devices. Among the tested structures, the 7% Ag-doped sample delivered the best photovoltaic performance with an efficiency of 0.3125, attributed to more substantial plasmonic effects, higher current generation, and optimized charge transport. The 5% Ag-doped device showed moderate performance (0.1027) due to a balance between morphology and electronic structure, while the 3% Ag-doped sample exhibited the smoothest surface and an efficiency of 0.964. These outcomes underscore the importance of optimizing doping levels to mitigate recombination and surface defects while leveraging localized surface plasmon resonance (LSPR) to enhance light absorption. The findings support the potential of Ag-doped ZnO/CuO-based heterojunctions for developing efficient and scalable optoelectronic devices.

Nomenclature	
Ag	Silver
AgNPs	Silver Nanoparticles
α	Absorption coefficient
CuO	Copper(II) oxide
D	Crystallite size (nm)
Eg	Optical band gap energy (eV)
FF	Fill Factor (%)

Nomenclature	
Ag	Silver
FWHM (β)	Full Width at Half Maximum (of XRD peak)
hν	Photon energy (eV)
I–V	Current–Voltage
Isc	Short-circuit current (μA)
Im	Current at maximum power point (μA)
K	Scherrer constant (shape factor, typically 0.94)
LSPR	Localized Surface Plasmon Resonance
NaOH	Sodium hydroxide
Pmax	Maximum output power (μW)
PLA	Pulsed Laser Ablation
PS	Porous Silicon
Sq	Root Mean Square Surface Roughness (nm)
Si	Silicon
UV-Vis	Ultraviolet-Visible Spectroscopy
Vm	Voltage at maximum power point (mV)
Voc	Open-circuit voltage (mV)
XRD	X-ray Diffraction
ZnO	Zinc Oxide
λ	X-ray wavelength (typically 1.5406 Å for Cu-Kα)
θ	Bragg angle (°)

References

1. Aadim, K. A., & Jasim, A. S. (2022). Silver nanoparticles synthesized by Nd: YAG laser ablation technique: characterization and antibacterial activity. Karbala International Journal of Modern Science, 8(1), 71–82. https://doi.org/10.33640/2405-609X.3210
2. Abdullah, S., Jaduaa, M., & Abd, A. N. (2021). Preparation of Bismuth Oxide Nanoparticles/PSi/Si heterojunction by a simple chemical method for solar cell applications. In Journal of Physics: Conference Series (Vol. 1853, No. 1, p. 012045). IOP Publishing. https://doi.org/10.1088/1742-6596/1853/1/012045
3. Alkhafaji, E. N., & Umran, N. M. (2024). Preparation and diagnosis of zinc oxide nano-hybrid composite with silver nanoparticles and study the kinetic release of silver nanoparticles. https://doi.org/10.21203/rs.3.rs-4799794/v1
4. Anandaraj, K., Ilakkiya, R., & Natarajan, N. (2018). Synthesis of zinc oxide (ZnO), silver (Ag), copper oxide (CuO) and titanium oxide (TiO2) nanoparticles. International Journal of Current Microbiology and Applied Sciences, 7(11), 1514–1521. http://dx.doi.org/10.20546/ijcmas.2018.711.174
5. Baran, T., Wojtyła, S., Dibenedetto, A., Aresta, M., & Macyk, W. (2021). Copper oxide-based photocatalysts and photocathodes: fundamentals and recent advances. Molecules, 26(23), Article 7271. https://doi.org/10.3390/molecules26237271
6. Bulutay, C., & Ossicini, S. (2010). Electronic and optical properties of silicon nanocrystals. In Silicon Nanocrystals (pp. 5–42). Wiley-VCH Verlag GmbH & Co. KGaA. https://doi.org/10.1002/9783527629954
7. Chen, K., Zhang, Y., Wang, X., Liu, H., & Li, M. (2025). Photocatalysis for sustainable energy and environmental protection in construction: A review on surface engineering and emerging synthesis. Journal of Environmental Chemical Engineering, 13(5), Article 117529. https://doi.org/10.1007/s13369-024-09941-3
8. Dorodnyy, A., Alarcon-Lladó, E., Shklover, V., Hafner, C., Fontcuberta i Morral, A., & Leuthold, J. (2018). Plasmonic photodetectors. IEEE Journal of Selected Topics in Quantum Electronics, 24(6), 1–13. https://doi.org/10.1109/JSTQE.2018.2840339
9. Fayyadh, A. A., & Alzubaidy, M. H. J. (2021). Biosynthesis and characterization of ZnO: Ag2O nanocomposite for antifungal efficacy. In Journal of Physics: Conference Series (Vol. 2114, No. 1, p. 012081). IOP

Publishing. https://doi.org/10.1088/1742-6596/2114/1/012081

10. Geim, A. K., & Novoselov, K. S. (2007). The rise of graphene. Nature Materials, 6(3), 183–191. https://doi.org/10.1038/nmat1849
11. Hassan, H. J., Jaber, A. A., & Thamer, A. (2025). Synthesis of ZnO nanorods through hydrothermal techniques: A study of optical properties and gas detection performance. Journal of Nanostructures, 15(3), 820–830. https://doi.org/10.22052/JNS.2025.03.001
12. Hoang, M. T., Nguyen, V. H., Le, T. K., Pham, Q. N., & Tran, D. L. (2025). Silver nanoparticles-decorated porous silicon microcavity as a high-performance SERS substrate for ultrasensitive detection of trace-level molecules. Nanomaterials, 15, Article 1007. https://doi.org/10.3390/nano15131007
13. Holzwarth, U., & Gibson, N. (2011). The Scherrer equation versus the 'Debye-Scherrer equation'. Nature Nanotechnology, 6(9), 534. https://doi.org/10.1038/nnano.2011.145
14. Khalifa, M., Jaduaa, M., & Abd, A. (2021). Al2O3 NPs/porous silicon/silicon photovoltaic device. In Journal of Physics: Conference Series (Vol. 1853, No. 1, p. 012046). IOP Publishing. https://doi.org/10.1088/1742-6596/1853/1/012046
15. Koppens, F. H. L., Mueller, T., Avouris, P., Ferrari, A. C., Vitiello, M. S., & Polini, M. (2014). Photodetectors based on graphene, other two-dimensional materials and hybrid systems. Nature Nanotechnology, 9(10), 780–793. https://doi.org/10.1038/nnano.2014.215
16. Lanje, A. S., Sharma, S. J., & Pode, R. B. (2010). Synthesis of silver nanoparticles: a safer alternative to conventional antimicrobial and antibacterial agents. Journal of Chemical and Pharmaceutical Research, 2(3), 478–483.
17. Lehmann, V. (2002). Electrochemistry of silicon: instrumentation, science, materials and applications.
18. Naderi, N., Ahmad, H., & Ismail, M. F. (2024). Improved optoelectrical performance of nanostructured ZnO/porous silicon photovoltaic devices. Ceramics International, 50(9, Part A), 14849-14855. https://doi.org/https://doi.org/10.1016/j.ceramint.2024.01.400
19. Alrasheedi, N. H. (2024). The Effects of Porous Silicon and Silicon Nitride Treatments on the Electronic Qualities of Multicrystalline Silicon for Solar Cell Applications. Silicon, 16(4), 1765-1773. https://doi.org/10.1007/s12633-023-02803-x
20. Hasani, E. (2025). Optimization of ZnO/CuO/Cu_2 Se heterojunction solar cells: a pathway to high efficiency via SCAPS-1D simulations. Optical and Quantum Electronics, 57(6), 361. https://doi.org/10.1007/s11082-025-08297-8
21. Nowsherwan, G. A., Samad, A., Iqbal, M. A., Mushtaq, T., Hussain, V., Akbar, M., Haider, S., Pham, P. V., & Choi, J. R. (2024). Advances in organic materials for next-generation optoelectronics: potential and challenges. Organics, 5(4), 520–560. https://doi.org/10.3390/org5040028
22. Özgür, Ü., Alivov, Y. I., Liu, C., Teke, A., Reshchikov, M. A., Doğan, S., Avrutin, V., Cho, S.-J., & Morkoć, H. (2005). A comprehensive review of ZnO materials and devices. Journal of Applied Physics, 98(4), Article 041301. https://doi.org/10.1063/1.1992666
23. Parekh, Z. R., Sharma, M., Prajapati, P. K., & Shimpi, N. G. (2021). CuO nanoparticles–synthesis by wet precipitation technique and their characterization. Physica B: Condensed Matter, 610, Article 412950. https://doi.org/10.1016/j.physb.2021.412950
24. Ra, H. S., Lee, A. Y., Kim, D. H., Cho, Y. J., Heo, J., & Lim, J. A. (2024). Advances in heterostructures for optoelectronic devices: materials, properties, conduction mechanisms, device applications. Small

Methods, 8(2), Article 2300245. https://doi.org/10.1002/smtd.202300245

25. Rocheleau, R. E., Miller, E. L., & Misra, A. (1998). High-efficiency photoelectrochemical hydrogen production using multijunction amorphous silicon photoelectrodes. Energy & Fuels, 12(1), 3–10. https://doi.org/10.1021/ef9701347
26. Suntako, R. (2015). Effect of zinc oxide nanoparticles synthesized by a precipitation method on mechanical and morphological properties of the CR foam. Bulletin of Materials Science, 38(4), 1033–1038. https://doi.org/10.1007/s12034-015-0921-0
27. Thamer, A. A., Imran, S. H., & Hassani, R. H. (2025). Sol-gel process optimization for CuO nanoparticle synthesis, achieving high purity and homogeneity. In Journal of Physics: Conference Series (Vol. 2974, No. 1, p. 012019). IOP Publishing. https://doi.org/10.1088/1742-6596/2974/1/012019
28. Tian, W., Zhang, C., Zhai, T., Li, S.-L., Wang, X., Liu, J., Jie, X., Liu, D., Liao, M., Koide, Y., Golberg, D., & Bando, Y. (2017). Hybrid nanostructures for photodetectors. Advanced Optical Materials, 5(4), Article 1600468. https://doi.org/10.1002/adom.201600468
29. Zainal Abidin, N. A., Asri, M. A., Teridi, M. A. M., Osman, N., Sopian, K., & Syafiq, A. (2023). Dopant engineering for ZnO electron transport layer towards efficient perovskite solar cells. RSC Advances, 13(48),33797–33819. https://doi.org/10.1039/D3RA04823C
30. Zielińska-Jurek, A. (2014). Progress, challenge, and perspective of bimetallic TiO2 ‐ based photocatalysts. Journal of Nanomaterials, 2014, Article 208920. https://doi.org/10.1155/2014/208920